Analytical Evaluation of the Asymptotic Impedance Matrix of a Grounded Dielectric Slab with Roof-Top Functions

Seong-Ook Park, Constantine A. Balanis, *Fellow, IEEE,* and Craig R. Birtcher

***Abstract*— In this paper, an analytical technique is derived to solve the asymptotic part of impedance matrix elements for printed circuit structures using roof-top subdomain expansions. The key to this problem is the analytical transformation from an infinite double integral to a suitable finite one-dimensional (1-D) integral. The newly developed formula is applied to the monostatic radar cross section (RCS) of a microstrip patch. Comparisons are made with measurements and conventional method of moments predictions.**

***Index Terms*—Impedance matrix, microstrip antennas.**

I. Introduction

RECENTLY, the authors [1] have successfully derived an analytical technique for evaluating the asymptotic part of the self and mutual interactions between the triangular-edge mode-basis functions along an electrically narrow strip. The method provides highly accurate results with minimal computational effort. However, the application of triangular-edge mode-basis functions, which have a vector field with only one component, is limited to problems similar to those of microstrip dipoles and discontinuities in narrow microstrip lines.

This paper presents an analytical technique to solve the asymptotic part of the impedance matrix in the spectral domain that employs roof-top subdomain basis functions to model surface current densities on a grounded dielectric slab. Roof-top subdomain basis functions are suitable for solving arbitrarily shaped planar geometries. However, the numerical evaluation of the integrals, without an acceleration technique, leads to very time-consuming computations.

Previously, Yang *et al.* [2] have presented an efficient numerical algorithm for directly evaluating the infinite double integral in the spectral domain. However, their method is incomplete because the efficient evaluation of the asymptotic part $\int_A^\infty \int_0^\infty \cdots dk_x\, dk_y$ was missing. Also, if the lateral separation (x_m and y_n of [2, Eq. (1)]) between the basis and testing functions becomes large, the efficiency decreases.

The formula presented in this paper produces accurate and efficient results for evaluating the asymptotic part of the impedance matrix without limitations. This results in a dramatic improvement in terms of the computation time for evaluating the impedance matrix elements. The formula derived is valid for any lateral separation between the two expansion functions. It is interesting that this method is especially more efficient in the case of the smaller size of the basis functions and larger lateral separations between the basis and testing functions, which is a pathological case of the conventional spectral domain analysis.

Manuscript received February 13, 1997; revised July 28, 1997. This work was supported by the U.S. Army Research Office under Contract DAAL 03-92-G-0262.

The authors are with the Department of Electrical Engineering, Telecommunications Research Center, Arizona State University, Tempe, AZ 85287 USA.

Publisher Item Identifier S 0018-926X(98)01494-X.

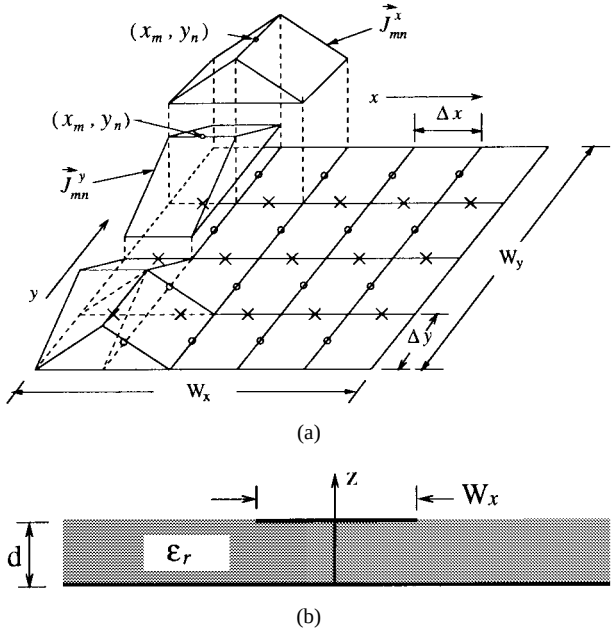

Fig. 1. Layout of roof-top basis functions on a microstrip patch.

II. Theory

Consider a perfectly conducting rectangular microstrip patch of dimensions $W_x \times W_y$ on a grounded dielectric substrate of thickness d and dielectric constant ϵ_r, as shown in Fig. 1.

In order to apply the moment method, we define the dyadic Green's function due to an infinitesimal current source on a grounded dielectric slab, which takes the form of [3], [4]

$$\tilde{G}_{xx}(k_x, k_y) = -j\frac{Z_0}{k_0}\frac{(\epsilon_r k_0^2 - k_x^2)k_2 + jk_1(k_0^2 - k_x^2)\tan(k_1 d)}{T_e T_m}\tan(k_1 d) \quad (1)$$

$$\tilde{G}_{yy}(k_x,k_y) = -j\frac{Z_0}{k_0}\frac{(\epsilon_r k_0^2 - k_y^2)k_2 + jk_1(k_0^2-k_y^2)\tan(k_1 d)}{T_e T_m}\tan(k_1 d) \tag{2}$$

$$\tilde{G}_{xy}(k_x,k_y) = \tilde{G}_{yx}(k_x,k_y) = j\frac{Z_0}{k_0}\frac{k_x k_y \tan(k_1 d)[k_2 + jk_1\tan(k_1 d)]}{T_e T_m} \tag{3}$$

where

$$\begin{aligned} T_e &= k_1 + jk_2\tan(k_1 d)\\ T_m &= \epsilon_r k_2 + jk_1\tan(k_1 d)\\ k_1^2 &= \epsilon_r k_0^2 - k_x^2 - k_y^2, \quad \mathrm{Im}\{k_1\}\le 0\\ k_2^2 &= k_0^2 - k_x^2 - k_y^2, \quad \mathrm{Im}\{k_2\}\le 0\\ \beta &= \sqrt{k_x^2+k_y^2} \end{aligned} \tag{4}$$

and $k_0 = \omega\sqrt{\mu_0\epsilon_0}$ where ω is the angular frequency and μ_0 and ϵ_0 are the permeability and permittivity of free-space, respectively.

The subscripts xy in $\tilde{G}_{xy}(k_x,k_y)$ represent an $\hat{x}$-directed electric field (in the form of a plane wave spectrum) due to an infinitesimal $\hat{y}$-directed current source. The subscripts of the other Green's functions have similar designations. The respective asymptotic Green's functions of (1)–(3), for large β are given by

$$\tilde{G}_{xx}^{\infty}(k_x,k_y) = -j\frac{Z_0}{k_0}\left\{\frac{k_0^2}{2\beta} - \frac{k_x^2}{(\epsilon_r+1)\beta}\right\} \tag{5}$$

$$\tilde{G}_{yy}^{\infty}(k_x,k_y) = -j\frac{Z_0}{k_0}\left\{\frac{k_0^2}{2\beta} - \frac{k_y^2}{(\epsilon_r+1)\beta}\right\} \tag{6}$$

$$\tilde{G}_{xy}^{\infty}(k_x,k_y) = \tilde{G}_{yx}^{\infty}(k_x,k_y) = j\frac{Z_0}{k_0}\frac{k_x k_y}{(\epsilon_r+1)\beta}. \tag{7}$$

In the next step, a set of roof-top subdomain basis functions are employed to model the current density distribution on the conductor. Roof-top functions are characterized by their triangular shape along the direction of current flow and rectangular cross section in the orthogonal direction. Thus, the current densities can be expressed as

$$J_{mn}^x(x,y) = \left(1 - \frac{|x-x_m|}{\Delta x}\right)\cdot \mathrm{rect}\left(\frac{y-y_n}{\Delta y}\right), \quad \frac{|x-x_m|}{\Delta x} < 1, \quad \frac{|y-y_n|}{\Delta y} < \frac{1}{2} \tag{8}$$

$$J_{mn}^y(x,y) = \mathrm{rect}\left(\frac{x-x_m}{\Delta x}\right)\cdot \left(1 - \frac{|y-y_n|}{\Delta y}\right), \quad \frac{|x-x_m|}{\Delta x} < \frac{1}{2}, \quad \frac{|y-y_n|}{\Delta y} < 1 \tag{9}$$

where

$$\mathrm{rect}\left(\frac{x}{L}\right) = \begin{cases} 1, & |x| < L/2\\ 0, & |x| > L/2. \end{cases}$$

The rectangular patch is divided into $(M+1)\times(N+1)$ cells along the $\hat{x}$ and $\hat{y}$ directions, with each cell having the dimensions of $\Delta x = W_x/(M+1)$ and $\Delta y = W_y/(N+1)$. The size of roof-top functions for the $\hat{x}$-directed current elements have dimensions $2\Delta x$ and Δy in the $\hat{x}$ and $\hat{y}$ directions, respectively, while the size of roof-top for the $\hat{y}$-directed current elements have dimensions Δx and $2\Delta y$.

The drawing in Fig. 1 illustrates the discretization and roof-top function layout for a rectangular patch. The centers of $\hat{x}$-directed roof-top functions are marked with circles and the centers of $\hat{y}$-directed functions are marked with crosses. To satisfy edge conditions and generate correct results, the centers between $\hat{x}$- and $\hat{y}$-directed currents need to be offset by $(\Delta x/2, \Delta y/2)$ [5].

The transforms of the $\hat{x}$- and $\hat{y}$-directed roof-top current densities of (8) and (9) can be written as

$$\tilde{J}_{mn}^x(k_x,k_y) = \frac{8}{\Delta x}\frac{\sin^2\left(k_x\frac{\Delta x}{2}\right)}{k_x^2}\frac{\sin\left(k_y\frac{\Delta y}{2}\right)}{k_y}e^{-j(k_x x_m + k_y y_n)} \tag{10}$$

$$\tilde{J}_{mn}^y(k_x,k_y) = \frac{8}{\Delta y}\frac{\sin\left(k_x\frac{\Delta x}{2}\right)}{k_x}\frac{\sin^2\left(k_y\frac{\Delta y}{2}\right)}{k_y^2}e^{-j(k_x x_m + k_y y_n)}. \tag{11}$$

The surface current densities can be expanded in terms of roof-top functions with an unknown set of current coefficients (I_{mn}^x, I_{mn}^y) as follows:

$$\tilde{J}_t^x(k_x,k_y) = \sum_{m=1}^{M}\sum_{n=1}^{N+1} I_{mn}^x \tilde{J}_{mn}^x(k_x,k_y) \tag{12}$$

$$\tilde{J}_t^y(k_x,k_y) = \sum_{m=1}^{M+1}\sum_{n=1}^{N} I_{mn}^y \tilde{J}_{mn}^y(k_x,k_y). \tag{13}$$

Using Galerkin's method, the impedance matrix elements in the spectral domain may be expressed in the form [1], [3]

$$\bar{\bar{Z}}_{mnm'n'} = -\frac{1}{4\pi^2}\int_{-\infty}^{\infty}\int_{-\infty}^{\infty}\vec{\tilde{J}}_{mn}(k_x,k_y)\bar{\bar{\tilde{G}}}(k_x,k_y) \times \vec{\tilde{J}}^{*}_{m'n'}(k_x,k_y)\,dk_x\,dk_y \tag{14}$$

where $mnm'n'$ represent the self and mutual interactions between the $\vec{\tilde{J}}_{mn}$ and $\vec{\tilde{J}}_{m'n'}$ current basis functions.

Employing the asymptotic extraction technique, (14) can be written as

$$\begin{aligned} \bar{\bar{Z}}_{mnm'n'} = &-\frac{1}{4\pi^2}\int_{-\infty}^{\infty}\int_{-\infty}^{\infty}\vec{\tilde{J}}_{mn}(k_x,k_y)[\bar{\bar{\tilde{G}}}(k_x,k_y)\\ &-\bar{\bar{\tilde{G}}}^{\infty}(k_x,k_y)]\vec{\tilde{J}}^{*}_{m'n'}(k_x,k_y)\,dk_x\,dk_y\\ &-\frac{1}{4\pi^2}\int_{-\infty}^{\infty}\int_{-\infty}^{\infty}\vec{\tilde{J}}_{mn}(k_x,k_y)\bar{\bar{\tilde{G}}}^{\infty}(k_x,k_y)\\ &\times\vec{\tilde{J}}^{*}_{m'n'}(k_x,k_y)\,dk_x\,dk_y. \end{aligned} \tag{15}$$

The first double integral in (15) converges more rapidly to zero than the double integral of (14). The integrand of the second infinite double integral in (15) exhibits slowly convergent and highly oscillatory behavior, which leads to difficulties when attempting to evaluate it using a direct numerical integration. Therefore, the main objective of this paper is to solve the second integral in (15) using an analytical technique.

III. Evaluation of Asymptotic Impedance Matrix

The asymptotic impedance matrix of the second integral in (15), associated with the roof-top functions of (10)–(11) and the asymptotic Green's function of (5)–(7), can be expressed as

$$Z_{mnm'n'}^{xx^{\mathrm{Asy}}} = -\frac{j}{\pi^2}\frac{Z_0}{k_0}\left(\frac{8}{\Delta x}\right)^2\left\{-\frac{k_0^2}{2}I_{mnm'n'}^{xx^a} + \frac{1}{(\epsilon_r+1)}I_{mnm'n'}^{xx^b}\right\} \tag{16}$$

$$Z_{mnm'n'}^{xy^{\mathrm{Asy}}} = Z_{mnm'n'}^{yx^{\mathrm{Asy}}} = \frac{j}{\pi^2}\frac{Z_0}{k_0}\left(\frac{64}{\Delta x\cdot\Delta y}\right)\frac{1}{\epsilon_r+1}I_{mnm'n'}^{xy} \tag{17}$$

with

$$I_{mnm'n'}^{xx^a} = \int_0^\infty\int_0^\infty \frac{\cos(k_x x_s)}{\sqrt{k_x^2+k_y^2}}\frac{\sin^2\left(k_y\frac{\Delta y}{2}\right)}{k_y^2} \times \frac{\sin^4\left(k_x\frac{\Delta x}{2}\right)}{k_x^4}\cos(k_y y_s)\,dk_x\,dk_y \tag{18}$$

$$I_{mnm'n'}^{xx^b} = \int_0^\infty\int_0^\infty \frac{\cos(k_x x_s)}{\sqrt{k_x^2+k_y^2}}\frac{\sin^2\left(k_y\frac{\Delta y}{2}\right)}{k_y^2} \times \frac{\sin^4\left(k_x\frac{\Delta x}{2}\right)}{k_x^2}\cos(k_y y_s)\,dk_x\,dk_y \tag{19}$$

$$I_{mnm'n'}^{xy} = -\int_0^\infty\int_0^\infty \frac{\sin(k_x x_s)}{\sqrt{k_x^2+k_y^2}}\frac{\sin^3\left(k_y\frac{\Delta x}{2}\right)}{k_x^2} \times \frac{\sin^3\left(k_y\frac{\Delta y}{2}\right)}{k_y^2}\sin(k_y y_s)\,dk_x\,dk_y \tag{20}$$

where the even and odd properties of the integrand are used to reduce the integration range in (18)–(20) and x_s and y_s (lateral separation distances) are defined as $(x_m - x_n)$ and $(y_m - y_n)$, respectively.

Both x_s and y_s in (18) and (19) have a discrete integer value of Δx and Δy, respectively. But x_s and y_s in (20) are represented by $\pm p\cdot\Delta x/2$ and $\pm q\cdot\Delta y/2$, respectively, where p and q may have odd numbers.

Each integrand in (18)–(20) is not separable in terms of k_x and k_y due to the $1/\sqrt{k_x^2+k_y^2}$ term, which prevents it from being reduced to the product of two one-dimensional (1-D) integrals. By introducing the same technique represented by [1, Eq. (11)], the integrals of (18)–(20) can be expressed as

$$I_{mnm'n'}^{xx^a} = \frac{1}{\pi}\int_{-\infty}^\infty\left\{\int_0^\infty K_0(k_y|\chi-x_s|)\frac{\sin^2\left(k_y\frac{\Delta y}{2}\right)}{k_y^2} \times\cos(k_y y_s)\,dk_y\int_0^\infty\frac{\sin^4\left(k_x\frac{\Delta x}{2}\right)}{k_x^4} \times\cos(k_x\chi)\,dk_x\right\}d\chi \tag{21}$$

$$I_{mnm'n'}^{xx^b} = \frac{1}{\pi}\int_{-\infty}^\infty\left\{\int_0^\infty K_0(k_y|\chi-x_s|)\frac{\sin^2\left(k_y\frac{\Delta y}{2}\right)}{k_y^2} \times\cos(k_y y_s)\,dk_y\int_0^\infty\frac{\sin^4\left(k_x\frac{\Delta x}{2}\right)}{k_x^2} \times\cos(k_x\chi)\,dk_x\right\}d\chi \tag{22}$$

$$I_{mnm'n'}^{xy} = -\frac{1}{\pi}\int_{-\infty}^\infty\int_0^\infty K_0(k_y\chi)\frac{\sin^3\left(k_y\frac{\Delta y}{2}\right)}{k_y^2} \times\sin(k_y y_s)\,dk_y\int_0^\infty\frac{\sin^3\left(k_x\frac{\Delta x}{2}\right)}{k_x^2}\sin(k_x x_s) \times\cos(k_x\chi)\,dk_x\,d\chi \tag{23}$$

where K_0 is the modified Bessel function of the first kind.

The infinite three-fold integrals of (21)–(23) can be converted into a 1-D integral if the separate integrals with respect to k_x and k_y can be evaluated in closed form. To accomplish this, the first integrals in (21)–(23) with respect to k_y are defined as

$$\mathcal{A}(\chi-x_s) = \int_0^\infty K_0(k_y|\chi-x_s|)\frac{\sin^2\left(k_y\frac{\Delta y}{2}\right)}{k_y^2}\cos(k_y y_s)\,dk_y \tag{24}$$

$$\mathcal{B}(\chi) = \int_0^\infty K_0(k_y\chi)\frac{\sin^3\left(k_y\frac{\Delta y}{2}\right)}{k_y^2}\sin(k_y y_s)\,dk_y \tag{25}$$

where $\mathcal{A}(\chi-x_s)$ and $\mathcal{B}(\chi)$ can be solved analytically. Their detailed derivations are presented in Appendixes A and B, respectively.

The second integrals in (21) and (22), with respect to k_x, were derived in [1, Eqs. (16), (17)] and each integral is rewritten as (26), as shown at the bottom of the next page

$$\Im_b(\chi) = \int_0^\infty\frac{\sin^4\left(k_x\frac{\Delta x}{2}\right)}{k_x^2}\cos(k_x\chi)\,dk_x = \begin{cases}\frac{\pi}{2}\left(\frac{1}{4}\Delta x-\frac{3}{8}\chi\right), & |\chi|<\Delta x\\ \frac{\pi}{2}\left(-\frac{1}{4}\Delta x+\frac{1}{8}\chi\right), & \Delta x\le|\chi|<2\Delta x\\ 0, & |\chi|\ge 2\Delta x.\end{cases} \tag{27}$$

Since $\Im_a(\chi)$ and $\Im_b(\chi)$ are compactly supported in the finite region $-2\Delta x<\chi<2\Delta x$, the infinite double integrals of (18) and (19) can be converted into finite 1-D integrals as follows:

$$I_{mnm'n'}^{xx^a} = \frac{1}{\pi}\int_{-2\Delta x}^{2\Delta x}\mathcal{A}(\chi-x_s)\cdot\Im_a(\chi)\,d\chi \tag{28}$$

$$I_{mnm'n'}^{xx^b} = \frac{1}{\pi}\int_{-2\Delta x}^{2\Delta x}\mathcal{A}(\chi-x_s)\cdot\Im_b(\chi)\,d\chi. \tag{29}$$

Similar expressions are obtained for $Z_{mnm'n'}^{yy^{\mathrm{Asy}}}$ by interchanging $\Delta x\leftrightarrow\Delta y$ and $x_s\leftrightarrow y_s$ in (16), (28), and (29). Each integrand in (28) and (29) has an integrable singularity at $\chi=x_s$ within the interval of integration if $x_s=0$ or $x_s=\pm\Delta x$ and $y_s=0$. Otherwise, each integrand is well behaved.

Next, let us consider the analytical solution of (23). By taking the derivative with respect to b on both sides of [6, formula 3.828.15] and changing the parameters, we introduce the following formula to evaluate (23):

$$\mathcal{T}(\chi) = \int_0^\infty\frac{\sin^3\left(k_x\frac{\Delta x}{2}\right)\sin(k_x\chi)}{k_x^2}\,dk_x = \begin{cases}-\frac{\pi}{8}\left(\frac{3\Delta x}{2}+\chi\right), & -\frac{3\Delta x}{2}<\chi<-\frac{\Delta x}{2}\\ \frac{\pi}{4}(\chi), & -\frac{\Delta x}{2}<\chi<\frac{\Delta x}{2}\\ \frac{\pi}{8}\left(\frac{3\Delta x}{2}-\chi\right), & \frac{\Delta x}{2}<\chi<\frac{3\Delta x}{2}\\ 0, & \text{otherwise.}\end{cases} \tag{30}$$

With the aid of (30), the second integral of (23) with respect to k_x is represented by

$$\Im_c(\chi) = \int_0^\infty \frac{\sin^3\left(k_x \frac{\Delta x}{2}\right)}{k_x^2} \sin(k_x x_s)\cos(k_x \chi)\, dk_x = \frac{1}{2}[\mathcal{T}(\chi + x_s) - \mathcal{T}(\chi - x_s)]. \tag{31}$$

With the aid of (25) and (31), (23) is reduced to

$$\begin{aligned} I^{xy}_{mnm'n'} &= -\frac{1}{2\pi}\int_{-\frac{3\Delta x}{2}-x_s}^{\frac{3\Delta x}{2}-x_s} \mathcal{B}(\chi)\cdot\mathcal{T}(\chi + x_s)\, d\chi \\ &\quad + \frac{1}{2\pi}\int_{-\frac{3\Delta x}{2}+x_s}^{\frac{3\Delta x}{2}+x_s} \mathcal{B}(\chi)\cdot\mathcal{T}(\chi - x_s)\, d\chi \\ &= \frac{1}{\pi}\int_{-\frac{3\Delta x}{2}+x_s}^{\frac{3\Delta x}{2}+x_s} \mathcal{B}(\chi)\cdot\mathcal{T}(\chi - x_s)\, d\chi \end{aligned} \tag{32}$$

where the even property of $\mathcal{B}(\chi)$ is used to reduce the two integrals to one integral.

Within the interval of integration, the integrand in (32) has an integrable singularity at $\chi = 0$ if $x_s = \pm\Delta x/2$ and $y_s = \pm\Delta y/2$ or $y_s = \pm 3\Delta y/2$. Since each integrand in (28), (29), and (32) has a logarithmic singularity, their integration at and near the singularity can be solved analytically at the local region of interest using the same procedure outlined in [1]. However, for convenience we use commonly available IMSL subroutines to integrate the finite 1-D integrals of (28), (29), and (32). If there is a singularity within the interval, the International Mathematics ans Statistics Library (IMSL) routine DQDAGP was used. If not, the IMSL routine DQDAGS was used, which is a general adaptive integral routine. The DQDAGP routine is a high-quality adaptive quadrature to handle endpoints as well as interior singularities.

If we look at the finite 1-D integrals of (28), (29), and (32) as counterparts corresponding to the double infinite integrals of (18), (19), and (20), we see that the interval of integration is determined only by the length of the basis function. This means that the smaller the size of the basis function, the more the interval of integration is reduced. Also if the lateral separation (x_s and y_s) between any two expansion functions becomes large, the behavior of the 1-D integrand becomes smoother. This smooth behavior allows us to evaluate the numerical integration faster and more accurately. In addition, since the integrand of the transformed 1-D integral does not lead to extra calculations, it is easier to compute.

It is interesting to examine two results—that obtained by the finite 1-D integrals and the other using the double infinite integrals. This allows direct comparisons between the two methods in terms of accuracy and execution time. As an example, the finite 1-D integrals of (28) and (29) are evaluated with $\Delta x = \Delta y = 1$ and $y_s = 2\cdot\Delta y$ for $0 \le x_s \le 10$ and (32) is evaluated with $\Delta x = \Delta y = 1$ and $y_s = 3\cdot\Delta y/2$. With these parameters, the two-dimensional (2-D) integrals of (18)–(20) are calculated with self-adaptive numerical quadratures with an upper truncation limit of $\beta^u = 300$ (rad/mm) and their accuracies are set up to four significant digits. The results are plotted in Fig. 2, which indicate excellent agreement. Because the results of the double infinite integral are computed numerically using a sufficiently large upper limit of truncation to give highly accurate results, this agreement verifies the validity of the newly derived formulas (28), (29), and (32).

Of particular interest are the execution times. While the computation time for the proposed method is not significantly affected by the separation distance x_s and y_s, the self-adaptive numerical integration of the 2-D integrals requires excessive computation time to achieve a comparable level of accuracy, if large lateral separation distances are to be analyzed. In this example, the average computation time to obtain the results of Fig. 2, using the proposed method, at each ten integer values of x_s, takes about $1/3000$ of the time required by the 2-D method while at the same time improving the accuracy.

IV. Measurement of RCS

To verify the developed analytical formulation, RCS measurements of a rectangular patch were made using RT/Duroid 5870, 0.078 74-cm thickness, 0.5-oz copper clad with dielectric constant of 2.33 ± 0.02 and a loss tangent of 0.0012 at 10 GHz.

The experimental data was collected on a compact antenna test range at Arizona State University. The measurements were made in four overlapping frequency bands corresponding to four sets of feed antennas: 3.7–6.4 GHz, 5.6–8.6 GHz, 7.8–12.8 GHz, and 12.0–18.4 GHz. The instrumentation is comprised of a vector network analyzer with a synthesized source. The source power was +11 dBm, the IF averaging factor was 2048, and 801 points were collected for each frequency band. The patch was cut by hand from adhesive-backed copper tape and burnished onto a 45.9 cm $\times$ 122.3 cm substrate.

For each frequency band, a multiple-step measurement procedure was employed. After calibrating the system to a 15.24-cm-diameter sphere, the substrate with the patch was mounted on an expanded polystyrene support structure on an azimuth over elevation positioner. The elevation axis of the positioner was rotated by 30° degrees so that the θ observation angle was 60°. The azimuthal axis of the positioner was rotated by 25° to reduce the backscatter of the substrate; the orientation of the patch was at 20° relative to the substrate for a ϕ observation angle of 45°.

$$\Im_a(\chi) = \int_0^\infty \frac{\sin^4\left(k_x \frac{\Delta x}{2}\right)}{k_x^4}\cos(k_x\chi)\, dk_x = \begin{cases} \frac{\pi}{96}\{(2\Delta x - |\chi|)^3 - 4(\Delta x - |\chi|)^3\}, & |\chi| < \Delta x \\ \frac{\pi}{96}(2\Delta x - |\chi|)^3, & \Delta x \le |\chi| < 2\Delta x \\ 0, & |\chi| \ge 2\Delta x \end{cases} \tag{26}$$

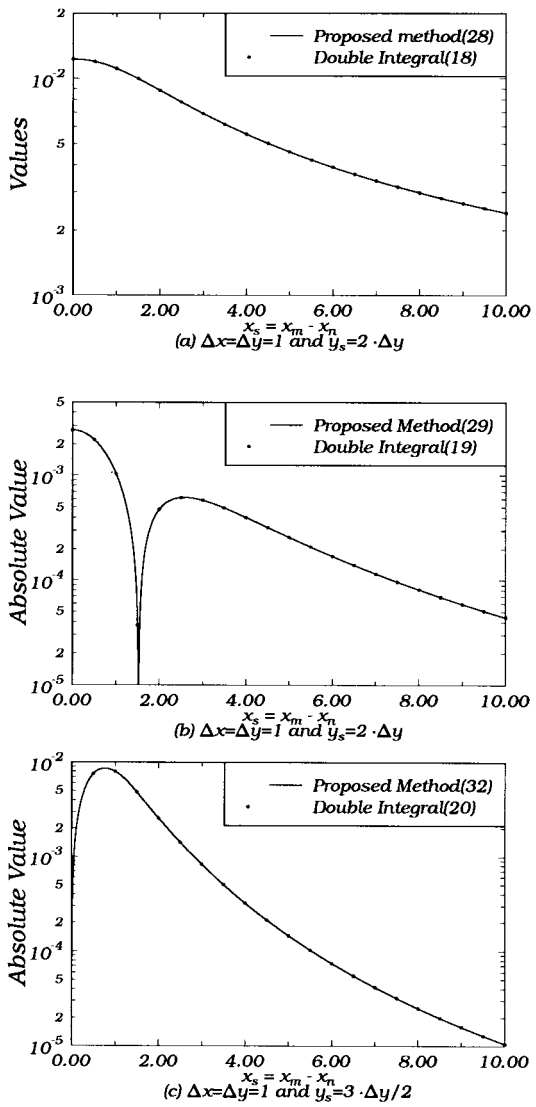

Fig. 2. Comparison between the infinite 2-D integral and the finite 1-D integral.

The response of the patch on the substrate was measured. The patch was removed, and the response of the empty substrate was measured. An approximation to the response of the patch in the presence of the substrate, but without the effects of the substrate edges, was obtained by subtracting the second measurement from the first. A time-domain gate was applied to the subtracted measurement to remove the effects of the residual responses of the substrate edges. Artifacts of the gating process were removed by clipping the ends of each frequency band. This process was repeated multiple times for each band. The individual measurements were very consistent, but the amplitude of two or more measurements were averaged together per frequency band to reduce small variations. This was particularly effective at frequencies above approximately 9 GHz.

V. Numerical Results of RCS

To verify the proposed method, computations were made and were compared with measurements and other available numerical data. The structure investigated is a 2-cm square patch on a grounded dielectric substrate of thickness $d = 0.078\,74$ cm and dielectric constant $\epsilon_r = 2.33$.

Enforcing the boundary condition on the surface of a perfectly conducting patch, the total tangential electric field (the sum of the incident and scattering electric fields) must be zero, i.e., $\vec{E}_{\tan}^{\text{scat}} + \vec{E}_{\tan}^{\text{inc}} = 0$. Using Galerkin's method, the electric field equation is reduced to the following matrix equation [7], [8]:

$$\begin{bmatrix} [Z^{xx}_{mnm'n'}] & [Z^{xy}_{mnm'n'}] \\ [Z^{yx}_{mnm'n'}] & [Z^{yy}_{mnm'n'}] \end{bmatrix} \begin{bmatrix} [I^{x}_{m'n'}] \\ [I^{y}_{m'n'}] \end{bmatrix} = \begin{bmatrix} [V^{x}_{mn}] \\ [V^{y}_{mn}] \end{bmatrix} \tag{33}$$

where each submatrix is described in (14) and the unknown coefficients of $I^x_{m'n'}$ and $I^y_{m'n'}$ are given in (12) and (13).

The excitation vector on the right side of (33) can be obtained by the inner product between the testing function and the incident field as

$$V_{mn} = \int_S \int \vec{J}_{mn} \cdot \vec{E}^{\text{inc}}\, dx\, dy. \tag{34}$$

Instead of performing the double integration directly to obtain (34), the excitation vector V_{mn} can be alternatively calculated by using the reciprocity theorem [9], [10]

$$V_{mn} = \frac{-4\pi \vec{E}_{mn} \cdot \vec{E}_0}{jw\mu_0} \tag{35}$$

where the $\vec{E}_{mn}$ is the far-field radiation due to the current density $\vec{J}_{mn}$ on the patch and $\vec{E}_0$ is the vector amplitude of the incident plane wave.

The far-zone field radiated by the expansion current densities J^x_{mn} and J^y_{mn} can be solved asymptotically by the method of stationary phase. The reader is referred to [9] and [10] for the expressions of the excitation vector.

Next, consider the evaluation of the matrix elements of (33). The double infinite integral in each submatrix is carried out by the asymptotic extraction technique described in (15). The first integral in (15) is performed numerically, after transforming into polar coordinates, with a finite upper limit β^u. The integrand of the first double integral in (15) possesses singularities corresponding to the surface wave poles. A number of techniques have been used to calculate these poles in the numerical integration such as a pole extraction technique [3], [11], a method of deformed integration contour [12], and a folding technique [13]. In this paper, these poles are evaluated with the use of a folding technique. After treating the singularities with the folding method, the remaining double integral of the first integral in (15) is performed using the IMSL routine DTWODQ, which is also an adaptive quadrature routine for double integration. In general, for the 2-D integrals, it was found that combining the folding technique and the IMSL routine DTWODQ provided sufficient accuracy.

The second integral in (15) is computed directly from the transformed 1-D integral over the finite integration region by using the adaptive integration algorithm. The direct double integration of the second integral in (15) is the most time consuming part of the overall computation of the matrix elements. Previously, to speed up this part, others [14], [15]

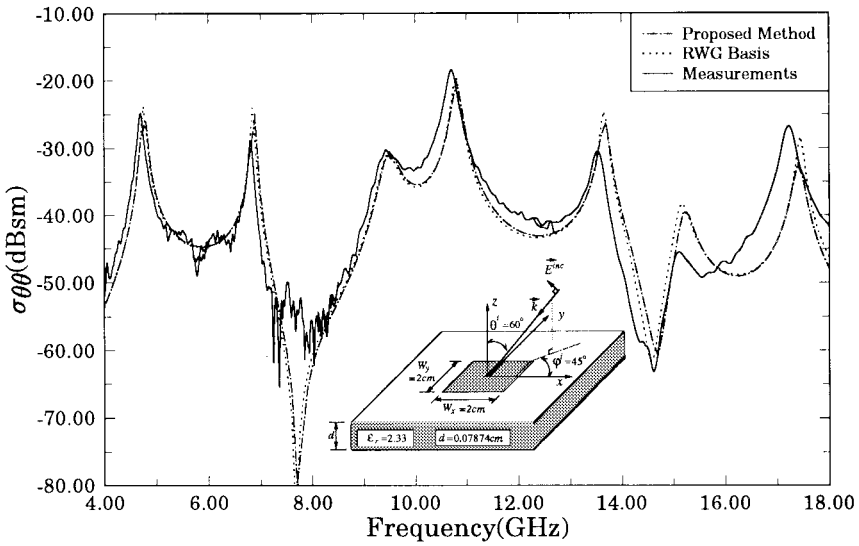

Fig. 3. Comparison between measured and predicted RCS.

have used the spatial domain method with the homogeneous Green's function, which results in a four-fold integral. This technique was originally developed by Pozar [14] and requires additional computations of the same geometry in a homogeneous medium. Thus, this method is still relatively time consuming. However, the calculation of this tail integral using the transformed finite 1-D integral has almost negligible computation time as compared to those of the first integral in (15).

An efficient algorithm for calculating the matrix element in (33) can take advantage of the occurrence of elements having repeated values as mentioned in [10]. The redundancies allow one to precompute the first row of each submatrix in $[Z^{xx}_{mnm'n'}]$, $[Z^{xy}_{mnm'n'}]$, and $[Z^{yy}_{mnm'n'}]$, and retrieve them later to fill the entire moment matrix. Also $[Z^{yx}_{mnm'n'}]$ can be obtained by rearranging $[Z^{xy}_{mnm'n'}]$.

The slowly varying nature of the impedance matrix elements over a wide-frequency range can be used to enhance the computational efficiency [8]. The impedance matrix elements are computed from a few sampled frequency points. The remaining impedance matrix elements at the intermediate frequency points are calculated using the cubic spline interpolation algorithm [16].

By using the above mentioned numerical techniques, the monostatic radar cross section (RCS) of a square microstrip patch is computed as a function of frequency for the incident angles $\phi^i = 45°$, $\theta^i = 60°$, with $\hat{\theta}$ polarization, and plotted in Fig. 3. As a check of the consistency and accuracy of the proposed method, our results are compared with the measured data as well as those using the Rao, Wilton, and Glisson (RWG) subdomain basis functions, which have 225 unknown coefficients [16]. Their respective results are included in Fig. 3. For the results of the method of this paper and RWG solution, there is a good agreement with each other over a wide range of frequencies.

The convergence of the solution was investigated by varying the number of subsections. The solution of our method converges relatively well by using $M = N = 12$. Also, no significant improvement in the numerical results was found by further increasing the number of M and N over the frequency range from 4 to 18 GHz. Thus, here we use $M = N = 13$, which leads to $364 = [M \cdot (N+1) + N \cdot (M+1)]$ unknown coefficients. To evaluate the first integral in (15), an upper limit $\beta^u = 50 \cdot k_0$ is used to obtain the results in Fig. 3. This leads to a good convergency. Further increases in the upper limit do not enhance the accuracy (up to four significant figures) over the entire frequency region.

As shown in Fig. 3, good agreement between the measured and the numerically computed data is observed for the lower frequencies, while for the high frequencies the agreement is less favorable. To find the possible explanation of this slight disagreement for the high-frequency region, each of the parameters such as patch size, substrate dielectric constant and thickness, substrate loss, and the incident angle were varied by small values commensurate with the physical tolerances of the structure. We found that small changes of incident angle (within 2%) and the losses do not play a significant role; therefore, the losses may even be neglected in this case. However, the RCS results are affected by the physical tolerance of the remaining parameters such as patch size, substrate dielectric constant, and thickness. Thus, these tolerances may contribute to the slight discrepancies between the measurements and the predicted data in the high-frequency region. As an example, a 1% increase of the patch size causes the entire curve from 13 to 18 GHz to be shifted downward by 150 MHz.

To illustrate the overall speed of the computation time, the CPU time between the proposed method and the conventional spectral domain approach (SDA) without acceleration to obtain the RCS at a single frequency of 4 GHz is compared. In Table I the CPU times are given for two different numbers of unknowns. Using the proposed method, the chosen upper limit of $50 \cdot k_0$ to evaluate the integral of the matrix elements allows the result to be accurate to four significant digits; the overall time to obtain the RCS at 4 GHz was 45 s with 180 unknowns. Without any acceleration, the conventional SDA does not lead

TABLE I
CPU TIME ON A HP735/125 WORKSTATION FOR THE CALCULATION OF RCS (PATCH SIZE 2 cm × 2 cm, $\epsilon_r = 2.33$, $d = 0.7874$ mm, $\phi^i = 45°$, $\theta^i = 60°$, $f = 4$ GHz)

Number of Unknown (M=N)	SDA without acceleration(a) (seconds)	Proposed Method(b) (seconds)	Speed Improvement $\frac{a}{b}$
180(M=9) (B^u)	553 ($300 \cdot k_0$)	68 ($50 \cdot k_0$)	8.1
364(M=13) (B^u)	2729 ($500 \cdot k_0$)	153 ($50 \cdot k_0$)	17.8

to this level of accuracy until the upper limit β^u reaches $300 \cdot k_0$. With this value of upper limit, approximately 553 sec were needed using 180 unknowns. If the number of unknowns is increased to 364, the small size of the basis functions in the conventional SDA requires an upper limit of $500 \cdot k_0$ to achieve comparable accuracy, as seen in Table I. The method of this paper does not require the upper limit to change, depending on the size of basis functions, and it is clearly more accurate than the conventional SDA due to the elimination of the truncation error.

VI. CONCLUSION

Utilization of the analytical transform method for the asymptotic impedance matrix element provides a significant improvement in the computation time over the conventional SDA in the evaluation of the radar cross section of a microstrip patch. In addition, the proposed method leads to highly accurate results even for a relatively small upper limit of truncation. The computed results were compared with those of other methods and with measured data over a wide range of frequencies. Although the newly derived formula was demonstrated for the RCS of a microstrip patch, this approach can be easily applied to any arbitrarily shaped planar circuit.

APPENDIX A

The integration $\mathcal{A}(\chi - x_s)$ over the k_y plane can be converted into an integration over the y plane by using Parseval's theorem

$$\begin{aligned}\mathcal{A}(\chi - x_s) &= \int_0^\infty K_0(k_y|\chi - x_s|)\frac{\sin^2\left(k_y\frac{\Delta y}{2}\right)}{k_y^2}\cos(k_y y_s)\,dk_y \\ &= \int_0^\infty F_1(k_y)\,F_2(k_y)\,dk_y = \pi\int_{-\infty}^\infty f_1(y)\,f_2(y)\,dy.\end{aligned} \tag{36}$$

Let us define $F_1(k_y) = K_0(k_y|\chi - x_s|)$ and $F_2(k_y) = \sin^2(k_y\frac{\Delta y}{2})\cos(k_y y_s)/k_y^2$. With the aid of [6, formula 6.671.14], $f_1(y)$ can be solved as

$$\begin{aligned}f_1(y) &= \frac{1}{2\pi}\int_{-\infty}^\infty K_0(k_y|\chi - x_s|)\cos(k_y y)\,dk_y \\ &= \frac{1}{2}\frac{1}{\sqrt{(\chi - x_s)^2 + y^2}}\end{aligned} \tag{37}$$

$f_2(y)$ can be easily obtained as

$$\begin{aligned}f_2(y) &= \frac{1}{2\pi}\int_{-\infty}^\infty \frac{\sin^2\left(k_y\frac{\Delta y}{2}\right)}{k_y^2}\cos(k_y y_s)\cos(k_y y)\,dk_y \\ &= \frac{\Delta y}{8}\Lambda\left(\frac{y + y_s}{\Delta y}\right) + \frac{\Delta y}{8}\Lambda\left(\frac{y - y_s}{\Delta y}\right)\end{aligned} \tag{38}$$

where

$$\Lambda\left(\frac{y}{\Delta y}\right) = \begin{cases}1 - \frac{|y|}{\Delta y}, & |y| < \Delta y \\ 0, & \text{otherwise.}\end{cases}$$

Substituting (37) and (38) into (36), $\mathcal{A}(\chi - x_s)$ can be represented analytically as

$$\begin{aligned}\mathcal{A}(\chi - x_s) = \pi\frac{\Delta y}{16}\int_{-\infty}^\infty &\frac{1}{\sqrt{(\chi - x_s)^2 + y^2}} \\ &\times\left[\Lambda\left(\frac{y + y_s}{\Delta y}\right) + \Lambda\left(\frac{y - y_s}{\Delta y}\right)\right]dy\end{aligned} \tag{39}$$

if $n = 0$

$$\begin{aligned}\mathcal{A}(\chi - x_s) = \pi\left(\frac{\Delta y}{4}\right)\Big\{&\ln\left(\Delta y + \sqrt{(\chi - x_s)^2 + \Delta y^2}\right) \\ &- \ln(|\chi - x_s|) - \frac{1}{\Delta y}\sqrt{(\chi - x_s)^2 + \Delta y^2} \\ &+ \frac{1}{\Delta y}|\chi - x_s|\Big\}\end{aligned} \tag{40}$$

if $n \geq 1$

$$\begin{aligned}\mathcal{A}(\chi - x_s) = \pi\left(\frac{\Delta y}{8}\right)\Big\{&(1 + n)\left\{\ln\left[(n + 1)\Delta y\right.\right. \\ &\left.\left. + \sqrt{(\chi - x_s)^2 + (n + 1)^2\Delta y^2}\right]\right\} \\ &- (1 - n)\left\{\ln\left[(n - 1)\Delta y\right.\right. \\ &\left.\left. + \sqrt{(\chi - x_s)^2 + (n - 1)^2\Delta y^2}\right]\right\} \\ &- 2n\cdot\ln\left[n\Delta y + \sqrt{(\chi - x_s)^2 + n^2\Delta y^2}\right] \\ &+ \frac{2}{\Delta y}\sqrt{(\chi - x_s)^2 + n^2\Delta y^2} \\ &- \frac{1}{\Delta y}\sqrt{(\chi - x_s)^2 + (n - 1)^2\Delta y^2} \\ &- \frac{1}{\Delta y}\sqrt{(\chi - x_s)^2 + (n + 1)^2\Delta y^2}\Big\}\end{aligned} \tag{41}$$

where $x_s = m\Delta x$ and $y_s = n\Delta y$.

APPENDIX B

The integration $\mathcal{B}(\chi)$ over the k_y plane can be converted into an integration over the y plane by using Parseval's theorem

$$\begin{aligned}\mathcal{B}(\chi) &= \int_0^\infty K_0(k_y\chi)\frac{\sin^3\left(k_y\frac{\Delta y}{2}\right)}{k_y^2}\sin(k_y y_s)\,dk_y \\ &= \int_0^\infty F_1(k_y)F_2(k_y)\,dk_y = \pi\int_{-\infty}^\infty f_1(y)f_2(y)\,dy.\end{aligned} \tag{42}$$

Let us define $F_1(k_y) = K_0(k_y\chi)$ and $F_2(k_y) = \sin^3(k_y\frac{\Delta y}{2})\sin(k_y y_s)/k_y^2$. With the aid of [6, formula 6.671.14], $f_1(y)$ can be solved as

$$f_1(y) = \frac{1}{2\pi}\int_{-\infty}^{\infty} K_0(k_y\chi)\cos(k_y y)\,dk_y = \frac{1}{2}\frac{1}{\sqrt{\chi^2+y^2}}. \tag{43}$$

Using the formula (30), $f_2(y)$ can be easily obtained as

$$f_2(y) = \frac{1}{2\pi}\int_{-\infty}^{\infty}\frac{\sin^3\left(k_y\frac{\Delta y}{2}\right)}{k_y^2}\sin(k_y y_s)\cos(k_y y)\,dk_y = \frac{1}{2\pi}[\mathcal{T}(y+y_s)-\mathcal{T}(y-y_s)]. \tag{44}$$

Substituting (43) and (44) into (42), $\mathcal{B}(\chi)$ can be represented analytically as

$$\begin{aligned}\mathcal{B}(\chi) &= \pi\int_{-\infty}^{\infty} f_1(y)\cdot f_2(y)\,dy \\ &= \frac{\pi}{16}\Bigg\{-3\sqrt{\chi^2+\left(\frac{\Delta y}{2}+y_s\right)^2} \\ &\quad +3\sqrt{\chi^2+\left(\frac{\Delta y}{2}-y_s\right)^2}+\sqrt{\chi^2+\left(\frac{3\Delta y}{2}+y_s\right)^2} \\ &\quad -\sqrt{\chi^2+\left(\frac{3\Delta y}{2}-y_s\right)^2}+3\left(\frac{\Delta y}{2}+y_s\right)\ln\left(\frac{\Delta y}{2}\right. \\ &\quad \left.+y_s+\sqrt{\chi^2+\left(\frac{\Delta y}{2}+y_s\right)^2}\right)-3\left(-\frac{\Delta y}{2}+y_s\right) \\ &\quad \times\ln\left(-\frac{\Delta y}{2}+y_s+\sqrt{\chi^2+\left(\frac{\Delta y}{2}-y_s\right)^2}\right) \\ &\quad +\left(-\frac{3\Delta y}{2}+y_s\right)\ln\left(-\frac{3\Delta y}{2}+y_s\right. \\ &\quad \left.+\sqrt{\chi^2+\left(\frac{3\Delta y}{2}-y_s\right)^2}\right)-\left(\frac{3\Delta y}{2}+y_s\right) \\ &\quad \times\ln\left(\frac{3\Delta y}{2}+y_s+\sqrt{\chi^2+\left(\frac{3\Delta y}{2}+y_s\right)^2}\right)\Bigg\}\end{aligned} \tag{45}$$

where $y_s = \pm q\Delta y/2$ (q: odd number).

ACKNOWLEDGMENT

The authors would like to thank Dr. J. T. Aberle for providing the comparison data and spline interpolation algorithm, Dr. J. F. Harvey of ARO, and Dr. J. W. Mink, formerly of ARO, for their interest and support of this project.

REFERENCES

[1] S.-O. Park and C. A. Balanis, "Analytical transform technique to evaluate the asymptotic part of impedance matrix of Sommerfeld-type integrals," *IEEE Trans. Antennas Propagat.*, vol. 45, pp. 798–805, May 1997.
[2] H.-Y. Yang, A. Nakatani, and J. A. Castañeda, "Efficient evaluation of spectral integrals in the moment method solution of microstrip antennas and circuits," *IEEE Trans. Antennas Propagat.*, vol. 38, pp. 1127–1129, July 1990.
[3] D. M. Pozar, "Input impedance and mutual coupling of rectangular microstrip antennas," *IEEE Trans. Antennas Propagat.*, vol. AP-30, pp. 1191–1196, Nov. 1982.
[4] R. W. Jackson and D. M. Pozar, "Full-wave analysis of microstrip open-end and gap discontinuities," *IEEE Trans. Microwave Theory Tech.*, vol. MTT-33, pp. 1036–1042, Oct. 1985.
[5] A. W. Glisson and D. R. Wilton, "Electromagnetic scattering by surfaces of arbitrary shape," *IEEE Trans. Antennas Propagat.*, vol. AP-28, pp. 593–603, Sept. 1980.
[6] I. S. Gradshteyn and I. M. Ryzhik, *Table of Integrals, Series, and Products*. New York: Academic, 1980.
[7] M. C. Bailey and M. D. Deshpande, "Integral equation formulation of microstrip antennas," *IEEE Trans. Antennas Propagat.*, vol. AP-30, pp. 651–656, July 1982.
[8] E. H. Newman and D. Forrai, "Scattering from a microstrip patch," *IEEE Trans. Antennas Propagat.*, vol. AP-35, pp. 245–251, Mar. 1987.
[9] D. R. Jackson, "The RCS of a rectangular microstrip patch in a substrate–superstrate geometry," *IEEE Trans. Antennas Propagat.*, vol. 38, pp. 2–8, Jan. 1990.
[10] D. G. Shively, "Analysis of resistive microstrip structures," Ph.D. dissertation, Arizona State University, Tempe, AZ, 1993.
[11] P. B. Katéhi and N. G. Alexópoulos, "Real axis integration of Sommerfeld integrals with application to printed circuit antennas," *J. Math. Phys.*, vol. 24, pp. 527–533, 1983.
[12] T. Becks and I. Wolff, "Improvements of spectral domain analysis techniques for arbitrary planar circuits," in *Directions in Electromagnetic Wave Modeling*, H. L. Bertoni and L. B. Felsen, Eds. New York: Plenum, 1991.
[13] G. W. G. Pan, J. Tan, and J. D. Murphy, "Full-wave analysis of microstrip floating-line discontinuities," *IEEE Trans. Electromagn. Compat.*, vol. 36, pp. 49–59, Feb. 1994.
[14] D. M. Pozar, "Improved computational efficiency for the method of moments solution of printed dipoles and patch," *Electromagn.*, vol. 3, pp. 299–309, 1983.
[15] T. S. Horng, W. E. McKinzie, and N. G. Alexopoulos, "Full-wave spectral-domain analysis of compensation of microstrip discontinuities using triangular subdomain functions," *IEEE Trans. Microwave Theory Tech.*, vol. 40, pp. 2137–2147, Dec. 1992.
[16] J. T. Aberle, Arizona State University, private communication.

Seong-Ook Park was born in KyungPook, Korea, on December, 1964. He received the B.S. degree in electrical engineering from KyungPook National University, Korea, in 1987, the M.S. degree in electrical engineering from the Korea Advanced Institute of Science and Technology, Seoul, in 1989, and the Ph.D. degree in electrical engineering from Arizona State University, Tempe, in 1997.

From March 1989 to August 1993, he was a Research Engineer with Korea Telecom, working with microwave systems and network. Later, he joined the Telecommunication Research Center at Arizona State University, Tempe, until September 1997. Since then he has joined the Korea Information and Telecommunications Graduate School, Taejon, Korea, as an Assistant Professor. His research interests include analytical and numerical techniques in the area of microwave integrated circuits.

Dr. Park is a member of Phi Kappa Phi.

Constantine A. Balanis (S'62–M'68–SM'74–F'86) received the B.S.E.E. degree from Virginia Tech, Blacksburg, in 1964, the M.E.E. degree from the University of Virginia, Charlottesville, in 1966, and the Ph.D. degree in electrical engineering from Ohio State University, Columbus, in 1969.

From 1964 to 1970, he was with NASA Langley Research Center, Hampton, VA, and from 1970 to 1983 he was with the Department of Electrical Engineering, West Virginia University, Morgantown, WV. Since 1983 he has been with the Department of Electrical Engineering, Arizona State University, Tempe, where he is now Regents' Professor and Director of the Telecommunications Research Center. His research interests are in low- and high-frequency computational methods for antennas, scattering, and penetration, transient analysis, control of coupling, and reduction of pulse distortion in interconnects for monolithic microwave and millimeter wave circuits and electronic packaging, and multipath propagation. He is the author of *Antenna Theory: Analysis and Design* (New York: Wiley, 1982, 1996) and *Advanced Engineering Electromagnetics* (New York: Wiley, 1989).

Dr. Balanis received the 1992 Special Professionalism Award from the IEEE Phoenix Section, the 1989 IEEE Region 6 Individual Achievement Award, and the 1987–1988 Graduate Teaching Excellence Award, School of Engineering, Arizona State University. He is a member of ASEE Sigma Xi, Electromagnetics Academy, Tau Beta Pi, Eta Kappa Nu, and Phi Kappa Phi. He has served as Associate Editor of the IEEE TRANSACTIONS ON ANTENNAS AND PROPAGATION (1974–1977) and the IEEE TRANSACTIONS ON GEOSCIENCE AND REMOTE SENSING (1981–1984), as an Editor of the newsletter for the IEEE Geoscience and Remote Sensing Society, and was the Distinguished Lecturer Program of the IEEE Antennas and Propagation Society (1988–1991). He was also a member of the AdCom of the IEEE Antennas and Propagation Society (1992–1995).

Craig R. Birtcher was born in Phoenix, AZ, on March 30, 1959. He received the B.S. and M.S. degrees (both in electrical engineering) from Arizona State University, Tempe, in 1983 and 1992, respectively.

He has been at Arizona State University since 1987, where he is now an Associate Research Specialist in charge of the Electromagnetic Anechoic Chamber (EMAC) Facility. His research interests include antenna and RCS measurement techniques, near-field to far-field (NF/FF) techniques, and the measurement of electrical properties of solids.